

A&A manuscript no.
(will be inserted by hand later)

Your thesaurus codes are:
03(03.13.2; 03.20.1; 13.07.2; 02.14.1)

ASTRONOMY
AND
ASTROPHYSICS

Image Reconstruction of COMPTEL 1.8 MeV ^{26}Al Line Data

J. Knödlse¹, D. Dixon⁷, K. Bennett⁵, H. Bloemen³, R. Diehl², W. Hermsen³, U. Oberlack⁶, J. Ryan⁴, V. Schönfelder², and P. von Ballmoos¹

¹Centre d'Etude Spatiale des Rayonnements, CNRS/UPS, B.P. 4346, 31028 Toulouse Cedex 4, France

²Max-Planck-Institut für extraterrestrische Physik, Postfach 1603, 85740 Garching, Germany

³SRON-Utrecht, Sorbonnelaan 2, 3584 CA Utrecht, The Netherlands

⁴Space Science Center, University of New Hampshire, Durham NH 03824, U.S.A.

⁵Astrophysics Division, ESTEC, ESA, 2200 AG Noordwijk, The Netherlands

⁶Astrophysics Laboratory, Columbia University, New York, NY 10027, U.S.A.

⁷Institute for Geophysics and Planetary Physics, University of California, Riverside, CA 92521, U.S.A.

Received ; accepted

Abstract. We present a new algorithm, called Multiresolution Regularized Expectation Maximization (MREM), for the reconstruction of γ -ray intensity maps from COMPTEL data. The algorithm is based on the iterative Richardson-Lucy scheme to which we added a wavelet thresholding step in order to eliminate image-noise in the reconstruction. The wavelet thresholding explicitly accounts for spatial correlations in the data, and adapts the angular resolution locally, depending on the significance of the signal in the data.

We compare the performance of MREM to that of the maximum entropy and the Richardson-Lucy algorithms by means of Monte-Carlo simulations of COMPTEL 1.809 MeV γ -ray line observations. The simulations demonstrate that the maximum entropy and Richardson-Lucy algorithms provide virtually identical reconstructions which are heavily disturbed by image noise. MREM largely suppresses this noise in the reconstructions, showing only the significant structures that are present in the data.

Application of MREM to COMPTEL 1.8 MeV γ -ray line data results in a 1.809 MeV sky map that is much smoother than the maximum entropy or Richardson-Lucy reconstructions presented previously. The essential features of this map are (1) an asymmetric galactic ridge emission reaching from $l \approx 45^\circ$ to $l \approx 240^\circ$, (2) a bright localised emission feature in the Cygnus region around $(l, b) \approx (80^\circ, 0^\circ)$, (3) two emission spots at $l = 317^\circ$ and $l = 332^\circ$ situated in the galactic plane, and (4) an extended emission region around $(l, b) \approx (160^\circ, 0^\circ)$. Comparison of the MREM map to the simulated reconstructions demonstrates that the 1.809 MeV emission is confined to the galactic plane.

Key words: Methods: data analysis – Techniques: image processing – Gamma rays: observations – nucleosynthesis

1. Introduction

Imaging the γ -ray sky at MeV energies by the COMPTEL telescope aboard the *Compton Gamma-Ray Observatory* (CGRO) presents a major methodological challenge. Registered events are dominated by instrumental background, and additionally, source signals are widespread over the event parameter space. Consequently, image recovery relies on a complex deconvolution procedure and on the accurate modelling of the instrumental background component. A maximum entropy algorithm has been employed extensively for the reconstruction of intensity maps from COMPTEL data (Strong et al. 1992). Recent examples of maximum entropy all-sky maps can be found in Strong et al. (1999) and Bloemen et al. (1999a) for galactic continuum emission or in Oberlack et al. (1996), Oberlack (1997) and Bloemen et al. (1999b) for 1.809 MeV γ -ray line radiation, attributed to the radioactive decay of ^{26}Al .

Simulations revealed a tendency of clumpy reconstruction of emission in our maximum entropy images, leading to artificial ‘hot spots’ of γ -ray emission in the reconstructions of diffuse emission distributions (Knödlse¹ et al. 1996). From the images alone, these ‘hot spots’ are indistinguishable from real point-like γ -ray sources, leading to considerable difficulties for the interpretation of the sky maps. Indeed, the assessment of the significance of individual ‘hot spots’ requires a substantial analysis effort, using simulations, Bootstrap analysis, and model fitting (e.g. Oberlack 1997).

We understand the image lumpiness as the result of the weak constraints that are imposed on individual image pixels by our data. COMPTEL images are usually

Send offprint requests to: Jürgen Knödlse¹

Correspondence to: knodlse¹@cesr.fr

reconstructed on a $1^\circ \times 1^\circ$ pixel grid in order to exploit the telescope's angular location accuracy for point sources. The fine pixelisation implies, however, that for weak diffuse emission, γ -ray intensities in individual pixels are generally not significant. Increasing the pixel size could in principle avoid this problem at the expense, however, of a reduced angular resolution. We want to notice that this is not a particular property of the maximum entropy algorithm, but of every method that is operating on a fixed grid of independent image pixels. Apparently, significance and angular resolution are intimately related quantities (this relation is more generally known as the *bias-variance tradeoff*).

Algorithms that rely on a pre-defined pixel grid require an a priori choice of the angular resolution (by defining the pixel size) without constraining the significance of the fluxes in individual image pixels. Alternatively, one may follow the opposite approach by choosing a priori the significance of image structures without constraining the angular resolution in the reconstruction. An implementation of such an algorithm was discussed by Piña & Puetter (1993) who introduced generalised image cells (called 'pixons') to correlate adjacent image pixels according to the signal strength. However, the application of Pixon based image reconstruction to COMPTEL 1.8 MeV did not provide satisfactory results (Knödlseider et al. 1996).

In this paper we present a new algorithm, called *Multiresolution Regularized Expectation Maximization* (MREM), which we developed in particular for the reconstruction of diffuse γ -ray emission. We combined an expectation maximization (EM) algorithm with a multi-resolution analysis based on wavelets, which explicitly accounts for spatial correlations in the reconstructed image. This leads to a convergent algorithm which automatically stops when the significant structure has been extracted from the data (by significant structure we mean structure that will not change much under perturbation of the data). The method requires an a priori choice of the significance level of emission structures while adapting the angular resolution according to the signal.

In the following we will present the MREM algorithm (§2) and illustrate its performance by means of simulations of COMPTEL observations (§3). The MREM algorithm is then applied for the reconstruction of an 1.809 MeV all-sky map based on COMPTEL data obtained between May 1991 to June 1996 (§4). This sky map will be compared to 1.8 MeV all-sky maps presented previously which have been derived by the maximum entropy method (Oberlack et al. 1996) or the Richardson-Lucy algorithm (Knödlseider et al. 1996). A more theoretical description of the MREM algorithm will be given in a separate paper (Dixon et al., in preparation).

2. The MREM algorithm

MREM is based on the Richardson-Lucy (RL) algorithm which has been proposed by Richardson (1972) and Lucy (1974) for the restoration of degraded images. Given an initial estimate f_j^0 for the image, RL iteratively improves this estimate using

$$f_j^{k+1} = f_j^k \left(\frac{\sum_{i=1}^N \frac{n_i}{e_i^k} R_{ij}}{\sum_{i=1}^N R_{ij}} \right) \quad (1)$$

(k denotes the iteration). R_{ij} is the instrumental response matrix which links the data space (indexed by i) to the image space (indexed by j). For a given image f_j^k and a given background model b_i , the expected number of counts in a data space cell is given by $e_i^k = \sum_{j=1}^M R_{ij} f_j^k + b_i$. The number of events observed in data space cell i is given by n_i . It is easily seen that Eq. (1) may be also written in the additive form

$$f_j^{k+1} = f_j^k + \delta f_j^k, \quad (2)$$

where

$$\delta f_j^k = f_j^k \left(\frac{\sum_{i=1}^N \left(\frac{n_i}{e_i^k} - 1 \right) R_{ij}}{\sum_{i=1}^N R_{ij}} \right) \quad (3)$$

is the additive RL correction.

Shepp & Vardi (1982) demonstrated that the Richardson-Lucy scheme is a special case of the expectation maximization (EM) algorithm (Dempster et al. 1977), and consequently it converges to the positively constrained maximum likelihood solution for Poisson data. Due to the slow convergence of the algorithm, several modifications have been proposed to accelerate convergence (Fessler & Hero 1994). For COMPTEL data we found that the ML-LINB-1 algorithm of Kaufman (1987) gives reasonable acceleration without degrading the reconstruction properties. For ML-LINB-1, Eq. (2) is replaced by

$$f_j^{k+1} = f_j^k + \lambda^k \delta f_j^k, \quad (4)$$

where λ^k is determined for each iteration using a line-search in order to maximise the likelihood for f_j^{k+1} subject to the constraint $\lambda^k \delta f_j^k > -f_j^k$ (this constraint ensures the positivity of the intensities).

It is obvious from Eqs. (2) to (4) that RL operates on a pre-defined pixel grid without any direct correlation between individual pixels. In particular, apart from the convolution with the transpose of the response matrix R_{ij} , there is nothing which prevents RL from matching the estimates e_i^k to the measurement n_i , and noise can easily propagate into the reconstruction where it is generally amplified.

For these reasons we added a multiresolution analysis to the iterative procedure which aims to correlate the image pixels and to extract only the significant structure from the data.

Each iteration of our MREM algorithm is composed of four steps: First, we evaluate the normalised correction map

$$\delta h_j^k = \frac{\sum_{i=1}^N \left(\frac{n_i}{e_i^k} - 1 \right) R_{ij}}{\sqrt{\sum_{i=1}^N \frac{R_{ij}^2}{e_i^k}}}, \quad (5)$$

for which $\text{Var}(\delta h_j^k) = 1$. Second, δh_j^k is transformed into the wavelet domain where it is represented by a set of wavelet coefficients w_m^l , l representing the scales, and m denoting the wavelet coefficients at this scale. At scales $l > 1$ ($l = 1$ represents a DC offset) the coefficients falling below a given threshold τ^l are zeroed by applying the operator

$$\eta(w, \tau^l) = \begin{cases} 0 & : |w| < \tau^l \\ w & : |w| \geq \tau^l \end{cases}. \quad (6)$$

This method is generally referred to as *wavelet thresholding* and has been proven successful for the removing of noise from a dataset without smoothing out sharp structures (Donoho 1993; Graps 1995). Backtransformation of the nonzero coefficients from the wavelet domain into the image domain provides then a *de-noised* correction map $\delta \hat{h}_j^k$. In compact matrix notation, the second step is given by

$$\delta \hat{h}^k = \mathbf{W}^T \eta \mathbf{W} \delta h^k \quad (7)$$

where \mathbf{W} is the discrete wavelet transform (throughout this paper we use the translation invariant ‘cycle spinning’ transformation of Coifman & Donoho (1995) and employ Coiflet wavelets with 4 parameters). Third, we calculate

$$\delta f_j^k = f_j^k \delta \hat{h}_j^k \left(\frac{\sqrt{\sum_{i=1}^N \frac{R_{ij}^2}{e_i^k}}}{\sum_{i=1}^N R_{ij}} \right), \quad (8)$$

which, in absence of any wavelet thresholding, is equivalent to the original RL correction map Eq. (3). In the last step, the previous estimate f_j^k is updated using Eq. (4). Due to the wavelet thresholding, positivity of the pixel intensities is not implicitly assured, and we explicitly require $f_j^{k+1} \geq f_\epsilon$ where f_ϵ is a negligible intensity level.

For efficient de-noising, the scale-dependent thresholds τ^l have to be related to the expected statistical noise σ^l in the wavelet domain at each scale. We estimate σ^l by simulations where we replace n_i in Eq. (5) by a Poisson derivate of e_i^k and transformation of the resulting ‘mock correction map’ into the wavelet domain. In this approach it is important that the statistical noise in the MREM correction map δh_j^k is independent of the pixel location j . For this reason we normalised δh_j^k so that $\text{Var}(\delta h_j^k) = 1$.

We define then $\tau^l = s \sigma^l$, where s specifies the significance level below which structures should be suppressed in the reconstruction. In the examples presented below we will

vary s between 2.5 and 3.5 in order to demonstrate the impact of the choice of s on the reconstructed images.

The final critical aspect of MREM is that we do not calculate corrections for all wavelet scales simultaneously. We begin by allowing in only corrections corresponding to the largest wavelet scale, with the other scales simply being zeroed out; thus our estimate in the initial iterations corresponds only to the average large scale structure in the map. Once this converges, we then admit corrections from the next smallest wavelet scale, allow it to converge, and so forth. The resulting reconstruction is the final product of the algorithm, which generally requires between 20 and 40 iterations for our data.

This procedure of progressively admitting smaller wavelets is crucial to the performance of MREM, and has some rather interesting ramifications which we shall discuss in detail in a subsequent paper (Dixon et al., in preparation). We briefly note here that its main purpose is to aid in the discrimination of noise-induced corrections from that structure which is ‘stable’ in the sense of being reproducible from different datasets. Examination of Eq. (3) indicates that if the estimates e_i^k are very different from the data n_i , the corresponding corrections will also be large. Ideally, we would like this to occur *only* if the correction corresponds to some statistically interesting structure, but for arbitrary e_i^k (e.g., the initial flat guess) this won’t be the case. By first converging to a coarse approximation, we get an estimate that is ‘close’ to the next coarsest approximation, which generally forces the noise-induced corrections at that next smallest scale to be small compared to those which we deem ‘interesting’. It is further interesting to note that the unregularised RL iteration tends to pick out the larger scale average structure first, only adding details in later iterations, and in this sense the progressive scale procedure dovetails nicely with the known characteristics of the iteration.

The de-noising using the wavelet transform has the desired property of introducing pixel-to-pixel correlations in the image where the correlation length depends on the amount of structure in the data. Regions of the sky with uniform emission will be represented by few large-scale wavelet coefficients, while point sources are represented by few small-scale coefficients. An important feature of our algorithm is that it is convergent. If all significant structure has been extracted from the data, where ‘significant’ is defined by the choice of s , the thresholding operator will zero all wavelet coefficients and consequently the correction map will be structureless. At this point, further iterations won’t alter the reconstructed image anymore, hence we stop the iterations.

3. Simulations

To illustrate the performance of MREM with respect to the maximum entropy (ME) and the Richardson-Lucy (RL) algorithms, we apply them to simulated COMP-

TEL observations of 1.809 MeV γ -ray line emission. The mock data that are used in the simulations are based on a two-component data space model, composed of the instrumental background and adopted models for the γ -ray line distribution for two typical cases: a smooth large-scale emission model, and a rather structured model with emission on many spatial scales. The instrumental response and background were calculated as expected for the combination of observation periods 0.1 – 522.5, corresponding to data taken between May 1991 to June 1996. From both components of the data space model mock datasets were created independently by means of a random number generator assuming Poisson noise. Both components were then added and images have been reconstructed from the combined mock dataset. For the reconstructions it has been assumed that the instrumental background is known precisely, hence the resulting images are not subject to possible systematic uncertainties of the employed background model. They are sensitive, however, to statistical uncertainties which are due to the particular data ‘realisation’ as obtained by the random sampling procedure. To illustrate this sensitivity, the same mock dataset has been used for the instrumental background component in all simulations.

The following 1.809 MeV model intensity distributions have been chosen. First, we use an exponential disk model, i.e. the intensity distribution that is expected if the galactic ^{26}Al mass density would follow a double exponential law with scale radius of $R_0 = 4.5$ kpc and scale height of $z_0 = 90$ pc. Model fitting has confirmed that these parameters provide a reasonable first-order description of 1.809 MeV emission (Knödlseider 1997). The total galactic ^{26}Al mass has been normalised to $3M_\odot$, a value slightly in excess from recent findings (e.g. Diehl et al. 1997). Second, the EGRET > 100 MeV all-sky map was taken as template for the 1.809 MeV intensity distribution. The 1.809 MeV intensity level of the map was adjusted to a plausible level by fitting the map to COMPTEL 1.8 MeV γ -ray line data. The first case testifies the response of the image reconstruction algorithms to a smooth intensity distribution while the second case represents probably a more realistic situation with structure on all spatial scales, from point-like to diffuse galactic plane emission.

3.1. Exponential disk model

The results of the exponential disk simulation are compiled in Fig. 1. For comparison, the intensity distribution of the exponential disk model is also shown. Since in our implementation ME and RL provide no criteria where to stop the iterative procedure, we used the correlation coefficient between the reconstruction and the model intensity map to determine the iteration which provides the smallest discrepancy to the model. This is the case after iteration 8 for ME and the accelerated RL algorithm.

Both the ME and the RL reconstructions clearly pick up the emission ridge along the galactic plane with the highest intensities found towards the central radian ($-30^\circ < l < 30^\circ$). The most striking difference between the model and the ME and RL reconstructions, however, is the lumpiness of the recovered sky maps. Although the emission follows in average the model intensity profile, it exhibits strong oscillations around this average, leading to ‘hot spots’ and emission gaps along the galactic plane. Indeed, these oscillations are already present in the first iterations of the reconstruction process and become more and more amplified with proceeding iterations. If the iterations are pursued beyond those shown in Fig. 1, the oscillations will break up, and the image will be composed of nearly isolated point sources (Knödlseider et al. 1996).

It is also interesting to recognise that the ME reconstruction is virtually identical to the RL reconstruction. The difference between both algorithms is that ME imposes an additional constraint on the reconstructed image in that it ‘pushes’ the image towards a ‘flat’ sky map – especially if the data are not very constraining. This results in systematically lower fluxes for the ME reconstructions with respect to RL, which can be seen from the intensity profiles in Fig. 1. If the ME iterations are proceeded further, and hence the entropy criterion is gradually weakened, the flux discrepancy between ME and RL disappears. For this reason we always use ‘high’ (e.g. 20-30) iterations when we determine fluxes from our ME sky maps.

In contrast to ME and RL, the MREM reconstructions provide rather smooth emission distributions. While some lumpiness remains for $s = 2.5$, the images obtained with $s = 3.0$ and 3.5 show no ‘hot spots’ or emission gaps. In particular, the longitude profile is reasonably well reproduced and obeys only small deviations from the model distribution. The most striking difference between the MREM sky maps and the model is the larger latitude extent of the reconstructions. This, however, is not surprising since the width of the exponential disk model of 2.7° (FWHM) is considerably smaller than the instrument’s angular resolution of 4° (FWHM) at 1.8 MeV (Schönfelder et al. 1993). Together with the weakness of the signal, this limits the achievable resolution in the reconstructions. Indeed, the width of the latitude profile depends on the selected significance level s , rising from 5.3° for $s = 2.5$ to 9.6° for $s = 3.5$. Obviously, the significance of the recovered emission features and the angular resolution are intimately related quantities. Note that the width of the latitude profiles obtained by ME and RL is 5.7° (FWHM), which is also considerably wider than that of the model.

To judge the quality of the reconstructed images we determine the 1.8 MeV γ -ray line residuals by means of a maximum likelihood ratio test (de Boer et al. 1992). For this purpose the sky maps of Fig. 1 are convolved into the COMPTEL data space and added to the instrumental background model. Residual emission is then searched by

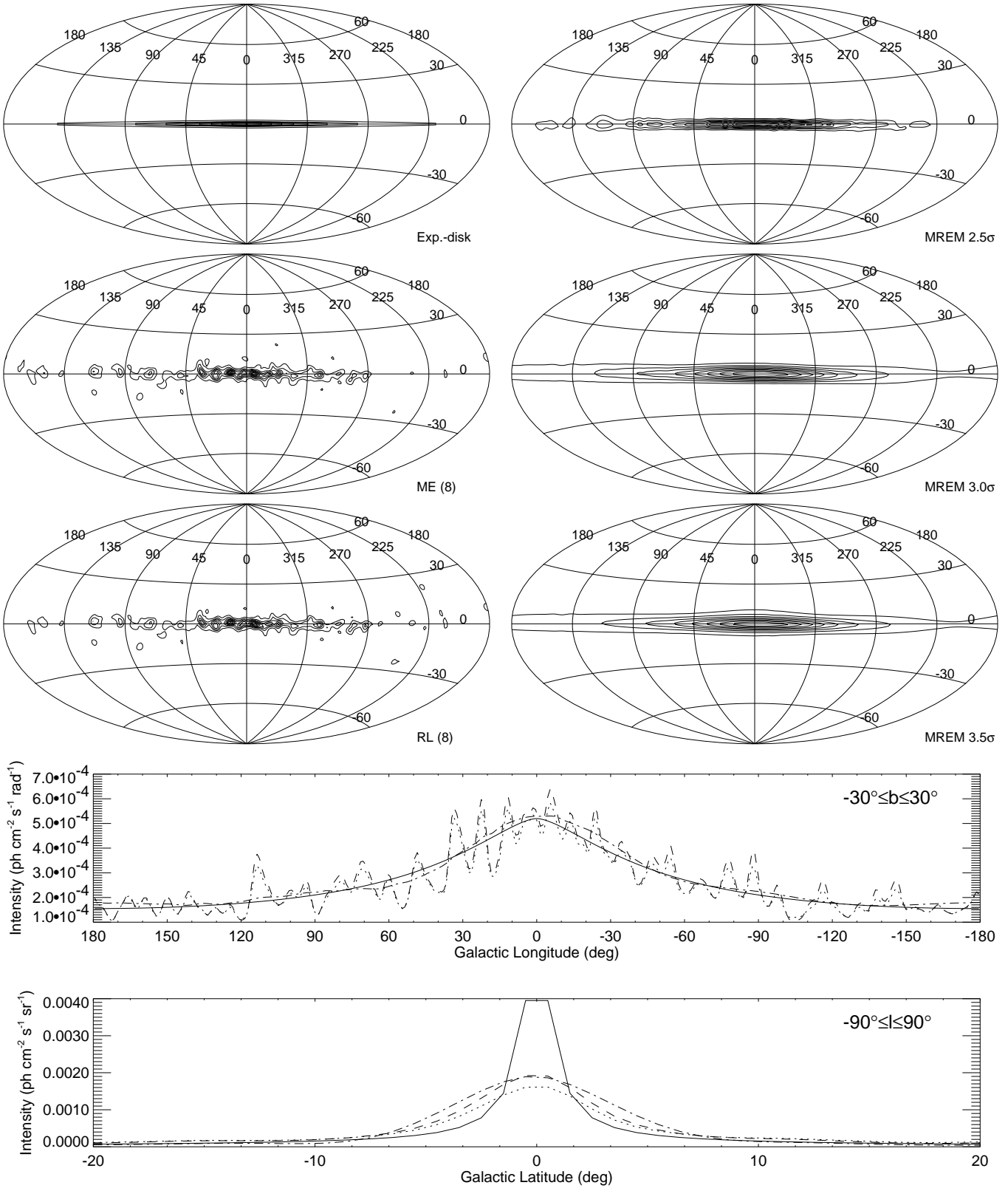


Fig. 1. Reconstruction of an exponential disk intensity distribution (Exp.-disk) using the maximum entropy method (ME), the Richardson-Lucy algorithm (RL), and the Multiresolution Regularized Expectation Maximization algorithm (MREM). MREM reconstructions for the significance levels $s = 2.5, 3.0,$ and 3.5 are shown. The bottom plots compare the longitude profile and latitude profile of the reconstructions to that of the exponential disk model; the model is shown as solid, the ME reconstruction as dotted, the RL reconstruction as dashed, and the MREM ($s = 3.0$) reconstruction as dashed-dotted line.

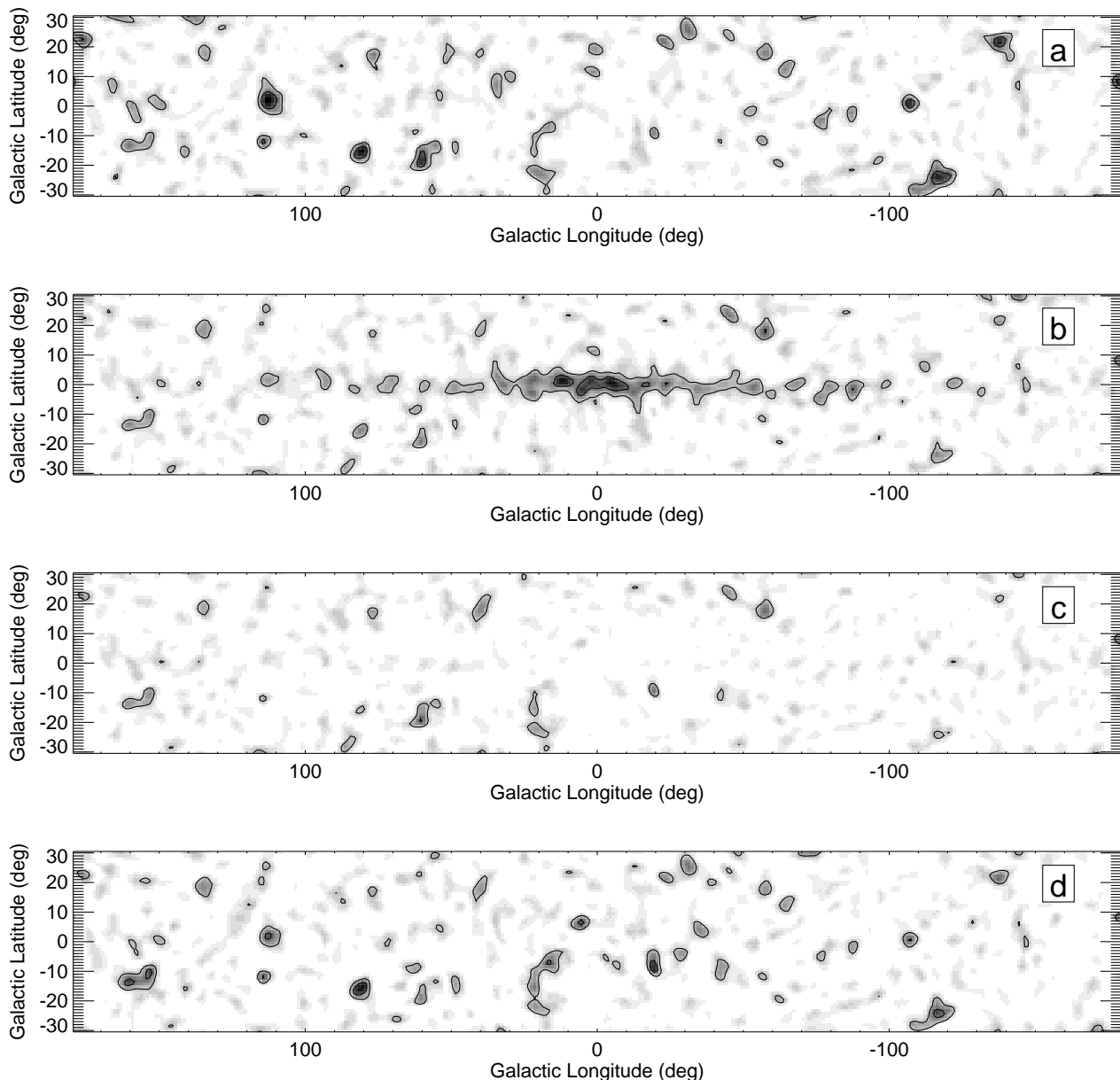


Fig. 2. Residual maximum likelihood ratio maps of the exponential disk simulations. Contour levels: $\sqrt{-2 \ln \lambda} = 2, 3, \dots$. From top to bottom the panels show (a) the residuals of the background sample only (i.e. the noise), (b) the residuals of iteration 8 of the ME reconstruction, (c) the residuals of iteration 8 of the RL reconstruction, and (d) the residuals of the MREM ($s = 3.0$) reconstruction.

fitting point source models on top of the combined data space model for a grid of source positions. The results of this point source search are shown in Fig. 2. The quantity plotted is $-2 \ln \lambda$, where λ is the maximum likelihood ratio $L(M)/L(S + M)$, M represents the (two-component) data space model, and S the source model which is moved over the sky area searched for residual emission. In such a search, $-2 \ln \lambda$ obeys a χ_3^2 distribution; in studies of a given source, χ_1^2 applies. In the latter case, the point source significance (in Gaussian σ) is given by $\sqrt{-2 \ln \lambda}$.

The top panel in Fig. 2 shows the residuals of the instrumental background sample only, hence reflects the statistical noise in the mock datasets (due to the dominance of the instrumental background component, the statistical noise is dominated by the background fluctuations). In the ideal case, the residuals of the reconstructed images should be almost identical to those of the background sample. Indeed, the residuals found on top of the MREM ($s = 3.0$) reconstruction (panel d) are very similar to those expected for an ideal reconstruction (panel a). The features are ba-

sically identical; only small deviations are found in their amplitude, e.g. at $l \approx 110^\circ$ where MREM slightly overestimates the emission. The ME reconstruction (panel b) forces image flatness, hence the residuals reflect a prominent flux suppression of the entire plane emission. We therefore cannot easily detect to which extent noise has been included in the ME reconstruction. For RL (panel c), no residual 1.8 MeV emission is seen that correlates with the galactic plane. In contrary, the likelihood ratios are even too small for the RL reconstruction with respect to the noise simulation, as expected if the data were overfit by the intensity map. Additionally, prominent background features, like those at $(l, b) = (113^\circ, 2^\circ)$ or at $(l, b) = (81^\circ, -16^\circ)$, are drastically reduced in both the ME and RL residual maps, yet are perceptible in the reconstructed intensity maps (cf. Fig. 1). This illustrates that statistical noise in the data is at least partially fit by the ME and RL sky maps. It follows that the lumpiness of the ME and RL reconstructions are due to overfitting of the data.

3.2. EGRET > 100 MeV sky map

Figure 3 presents the results of the simulations based on the EGRET > 100 MeV all-sky map. This map shows a ridge of diffuse emission along the galactic plane with a notably intensity enhancement towards the inner Galaxy, some prominent galactic point sources, some localised emission regions, and some extragalactic point sources. The intensity level of the EGRET > 100 MeV all-sky map has been adjusted to a plausible 1.8 MeV intensity level by fitting the map to COMPTEL 1.8 MeV γ -ray line data, resulting in a 1.809 MeV line flux from the inner radian ($|b| < 20^\circ$) of $\sim 3 \times 10^{-4}$ ph cm $^{-2}$ s $^{-1}$ rad $^{-1}$. This adjustment pushed most of the point sources in the EGRET map below the sensitivity limit of COMPTEL at 1.8 MeV, leaving Vela with 3×10^{-5} ph cm $^{-2}$ s $^{-1}$ and Geminga with 1×10^{-5} ph cm $^{-2}$ s $^{-1}$ as the most prominent objects.

Indeed, the only point source recovered in the ME and RL reconstructions is Vela ($l = 264^\circ$, $b = -3^\circ$), while only a small hint of γ -ray emission is seen at the position of Geminga ($l = 195^\circ$, $b = -4^\circ$). Similar to the exponential disk simulation, ‘hot spots’ and emission gaps appear along the galactic plane which only occasionally coincide with localised features in the model map. Such coincidences are found e.g. at $l \approx 80^\circ$ (Cygnus) or at $l \approx -45^\circ$. However, localised emission features are also found in the exponential disk simulations at these positions (cf. Fig. 1) where no such features are present in the model. Since only the mock dataset of the (dominant) instrumental background component is common to both simulations, it is very suggestive that the observed features are at least partially due to positive statistical fluctuations of the background data. Other localised emission features in the EGRET map, like the spots at $l \approx 20^\circ$, $l \approx -18^\circ$, or $l \approx -75^\circ$ (Carina), coincide with negative

statistical fluctuations of the background component and annihilate; consequently no feature is seen in the reconstructions at these positions. Additionally, artificial ‘hot spots’ appear in the ME and RL maps where no such features are present in the model. Examples are the strong feature at $l \approx 115^\circ$ and the spur towards negative latitudes at $l \approx -15^\circ$. Again, these features can also be perceived in the exponential disk simulations, confirming that they arise from the statistical noise of the background sample.

In contrast to ME and RL, MREM again provides much smoother reconstructions of the data, avoiding most of the artifacts. In the $s = 2.5$ run, only the most prominent artifacts are visible (e.g. the spot at $l \approx 115^\circ$), but many of the real localised features are recovered ($l \approx 80^\circ$, $l \approx 135^\circ$, $l \approx -45^\circ$, and Vela). Increasing the requirement for the significance of the emission structures to $s = 3.0$ removes the remaining artifacts, but eliminates also most of the localised emission features. Nevertheless, weak hints for Vela and the $l \approx 135^\circ$ source are still present in the sky map. These hints disappear when s is increased to 3.5. Again, the latitude extent of the reconstructions is slightly higher than that of the models due to the combined result of the instrument’s angular resolution of only 4° (FWHM) together with a low signal to noise ratio. Yet, the extended diffuse emission above the galactic centre is still recovered in the maps.

The residual analysis of the MREM $s = 3.0$ reconstruction reveals only weak emission at the position of the localised features, indicating that they are not very significant (cf. Fig. 4). The most prominent residuals are found at the position of Vela and at $(l, b) = (81^\circ, -16^\circ)$, with likelihood ratios of $-2 \ln \lambda = 16.6$ and 14.3, respectively. While the first residual corresponds to a real source in the EGRET map, the second one is a clear background fluctuation. If the existence of the Vela source would not be known a priori, the likelihood ratio of 16.6 converts to a detection significance of 3.3σ (3 d.o.f.). Taking into account the number of trials made in the point source search, this value can not be interpreted as a significant detection. However, if the Vela source is considered as known object, the likelihood ratio converts to a 4.1σ detection significance (1 d.o.f.). The major objective of an 1.809 MeV all-sky map, however, is the discovery of unknown objects, hence it is desirable that the Vela source is not recovered in the reconstruction. Otherwise, as demonstrated by the ME and RL or the MREM ($s = 2.5$) reconstructions, artifacts will also enter the reconstruction, making the interpretation of the sky map difficult.

To illustrate that MREM indeed recovers point sources if they are significant, we performed an additional simulation where we increased the intensity of the EGRET > 100 MeV template by a factor of 5 with respect to the 1.809 MeV intensity. This corresponds to an increase of a factor of 5 in the signal-to-noise ratio, which is equivalent to a sensitivity enhancement of the same magnitude. The resulting MREM reconstruction is shown in Fig. 5

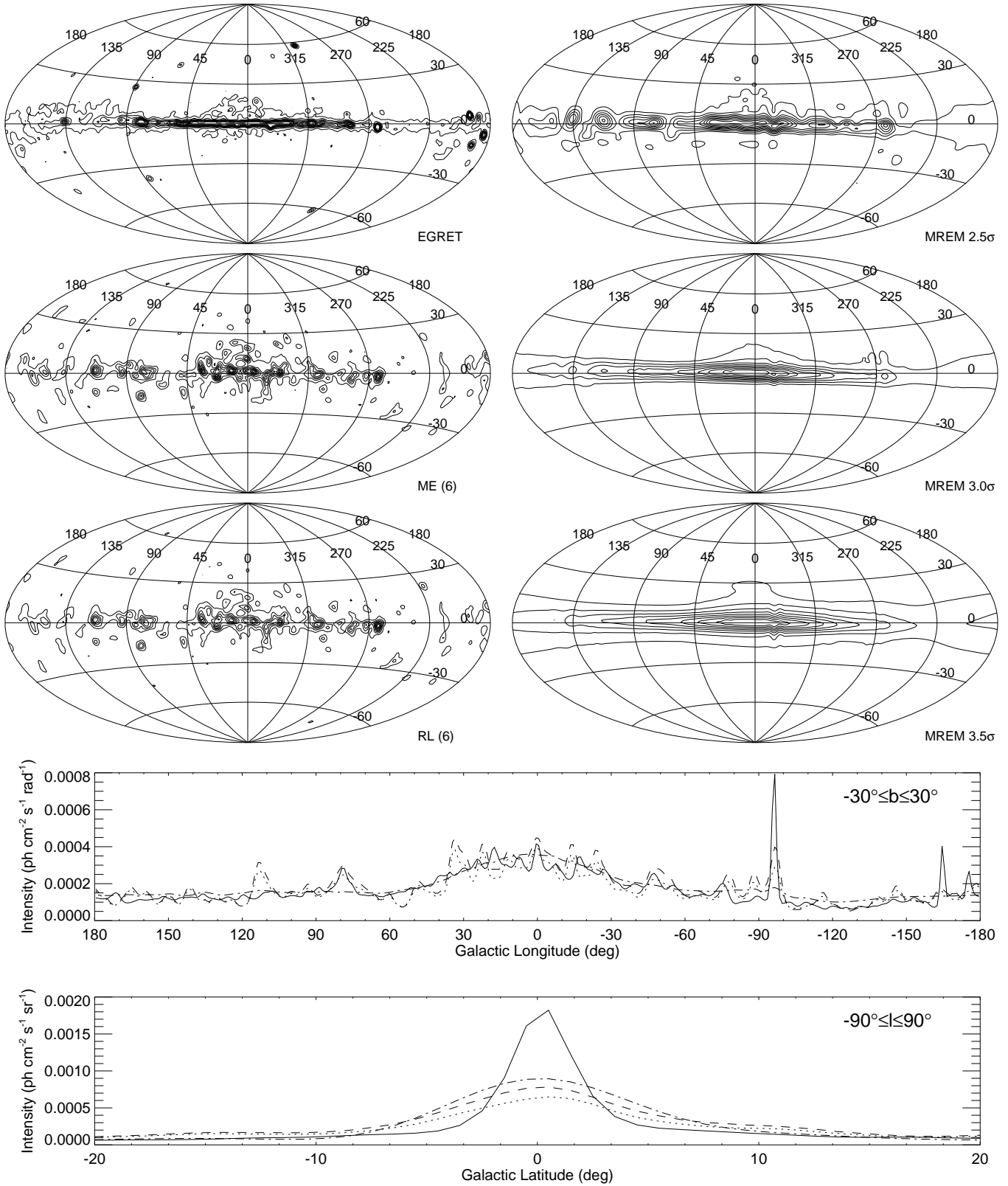


Fig. 3. Reconstruction of an EGRET > 100 MeV template which was adjusted to the expected 1.8 MeV intensity by means of a model fit. In the profiles, the model is shown as solid, the ME reconstruction as dotted, the RL reconstruction as dashed, and the MREM ($s = 3.0$) reconstruction as dashed-dotted line.

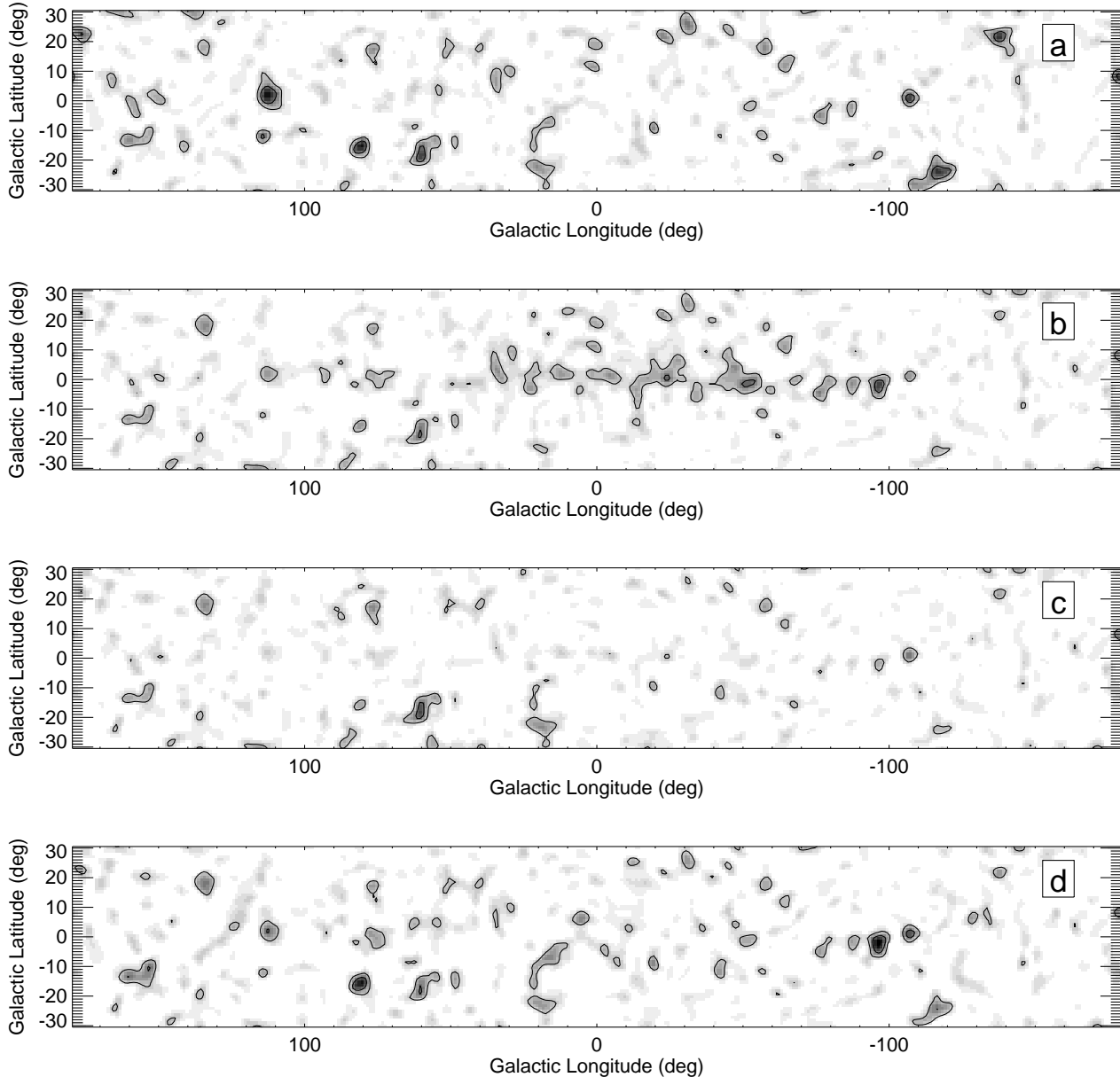


Fig. 4. Residual maximum likelihood ratio maps of the EGRET > 100 MeV all-sky map simulations. Contour levels like in Fig. 2. From top to bottom the panels show (a) the residuals of the background sample only (i.e. the noise), (b) the residuals of iteration 6 of the ME reconstruction, (c) the residuals of iteration 6 of the RL reconstruction, and (d) the residuals of the MREM ($s = 3.0$) reconstruction.

for $s = 3.0$. As expected, much more structure along the galactic plane is now recovered. Prominent point sources, such as Vela, Geminga, or the Crab, and localised emission features, e.g. in Cygnus and Carina, are now clearly visible. This demonstrates that the absence of these features in the MREM map derived for the 1.809 MeV intensity level (Fig. 3) relates to their significance.

4. The COMPTEL 1.8 MeV sky

The MREM algorithm is now applied to real COMPTEL 1.8 MeV data, taken during observation periods 0.1 - 522.5 (May 1991 to June 1996). The instrumental background component was estimated using contemporaneous data at adjacent energies, following the procedure described in Knödlseher et al. (1996). The time-variability of the instrumental background was taken into account by determination of the background model on single observation basis, and by its proper relative normalisation using

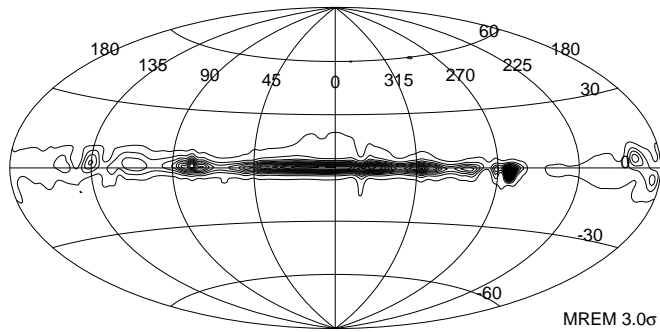


Fig. 5. MREM ($s = 3.0$) reconstruction of an EGRET > 100 MeV template with an intensity that is 5 times larger than the 1.809 MeV intensity.

the activation history of major background components (Oberlack 1997). Since the absolute normalisation as well as the $\bar{\varphi}$ distribution of the background model are only weakly constrained, we added an additional step where we determine both by all-sky model fitting (maximum likelihood optimisation). For this purpose we fitted the instrumental background model together with a template for the 1.809 MeV intensity distribution to the COMPTEL 1.8 MeV data, where we determined independent scaling factors for all $\bar{\varphi}$ layers of the background model as well as a global scaling factor for the 1.8 MeV intensity template. This procedure provides an estimate of the total 1.809 MeV sky flux and an improved estimate of the instrumental background component, which is then used for image reconstruction. For the 1.809 MeV template we used the 53 GHz free-free emission map derived from COBE/DMR data (Bennett et al. 1992) which was found to provide the best description of the COMPTEL 1.8 MeV data in a recent study using a wide variety of models (Knödlseher et al. 1999). An alternative method for deriving an instrumental background model for the analysis of 1.8 MeV γ -ray line data is described in Bloemen et al. (1999b).

Figure 6 shows the COMPTEL 1.809 MeV γ -ray line all-sky maps that are obtained by the different reconstruction algorithms. The maximum entropy and Richardson-Lucy maps are similar to those presented in previous work (Diehl et al. 1995; Oberlack et al. 1996; Knödlseher et al. 1996; Oberlack 1997; Bloemen et al. 1999b) with minor differences being due to differences in the analysed data volume or the employed background modelling procedure. The most distinct feature in these maps is emission along the ridge of the galactic plane. Again we see the lumpiness that our above simulations also show for these methods, indicating overfitting of the data. According to the discussion above we cannot decide from the sky maps alone which of the lumps may correspond to real emission and which are artifacts due to the background noise.

MREM avoids this confusion, suppressing efficiently the noise components of the image. The reconstructed intensity profiles are characterised by a notable asymme-

try with respect to the galactic centre and some localised emission features. The most prominent of these features is located in the Cygnus region around $(l, b) \approx (80^\circ, 0^\circ)$ where a bright extended emission spot is clearly separated from the inner galactic ridge emission by a bridge of relatively low 1.8 MeV intensity. The same feature is also seen in the ME and RL maps where it obeys a much more complex structure. The MREM reconstructions suggest that most of this structure is not individually significant, and could as well be more diffuse or located differently. We therefore safely may extract the fact of significant Cygnus region emission, separated from the inner galactic ridge.

This inner ridge appears smooth on the MREM image, yet also here reveals a pronounced asymmetry with respect to the galactic centre. While at positive longitudes the intensity drops steeply from $l \approx 30^\circ$ to $l \approx 50^\circ$, the 1.8 MeV emission extends continuously to $l \approx 240^\circ$ at negative longitudes. Along the ridge the MREM reconstructions reveal only little structure. From the many ‘hot spots’ seen in the ME and RL reconstructions, only the most prominent ones are still perceptible in the MREM image obtained for $s = 2.5$. Increasing the significance level to $s = 3.0$ removes most of them, keeping only two emission spots at $l = 317^\circ$ and 332° which are separated by a weak emission gap at $l = 324^\circ$. This is the most persistent structure along the inner galactic plane ridge which is still clearly visible for a significance level of $s = 3.5$. It is also very pronounced in the ME and RL maps. Additional hints for weak excess emission are found in the longitude profile at $l = 21^\circ, 30^\circ, 44^\circ, 286^\circ$, and 345° , but they disappear if s is increased to 3.5. Obviously, the significance of these excesses is close to the sensitivity limit of COMPTEL, and the assessment of their reality needs more dedicated studies.

The distinct emission gap which separates two localised emission regions at $l = 266^\circ$ (Vela) and $l = 286^\circ$ (Carina) in the ME and RL maps is not seen in the MREM reconstructions. Yet, a weak intensity dip is found in the $s = 2.5$ and 3.0 MREM maps at this location, indicating that some structure may indeed be present. The prominent ‘hot spot’ towards the galactic centre, clearly visible in the ME and RL maps at $l = 4^\circ$, is only present in the MREM map for $s = 2.5$, but disappears for higher significance levels. Apparently, the data are also consistent with a smooth emission profile in this region.

Comparison of the 1.8 MeV maps with the EGRET map simulations indicates that the 1.809 MeV emission is very confined to the galactic plane. In particular, there is no hint for an extended emission component similar to that seen in the EGRET map above the inner Galaxy. Indeed, model fitting using exponential disk models revealed a small scale height of $z_0 = 90$ pc for the galactic ^{26}Al distribution (Knödlseher 1997). Comparison of the 1.8 MeV maps with the exponential disk simulations (for which a scale height of $z_0 = 90$ pc was assumed) confirms this result. In particular, the width of the MREM ($s = 3.0$) 1.8

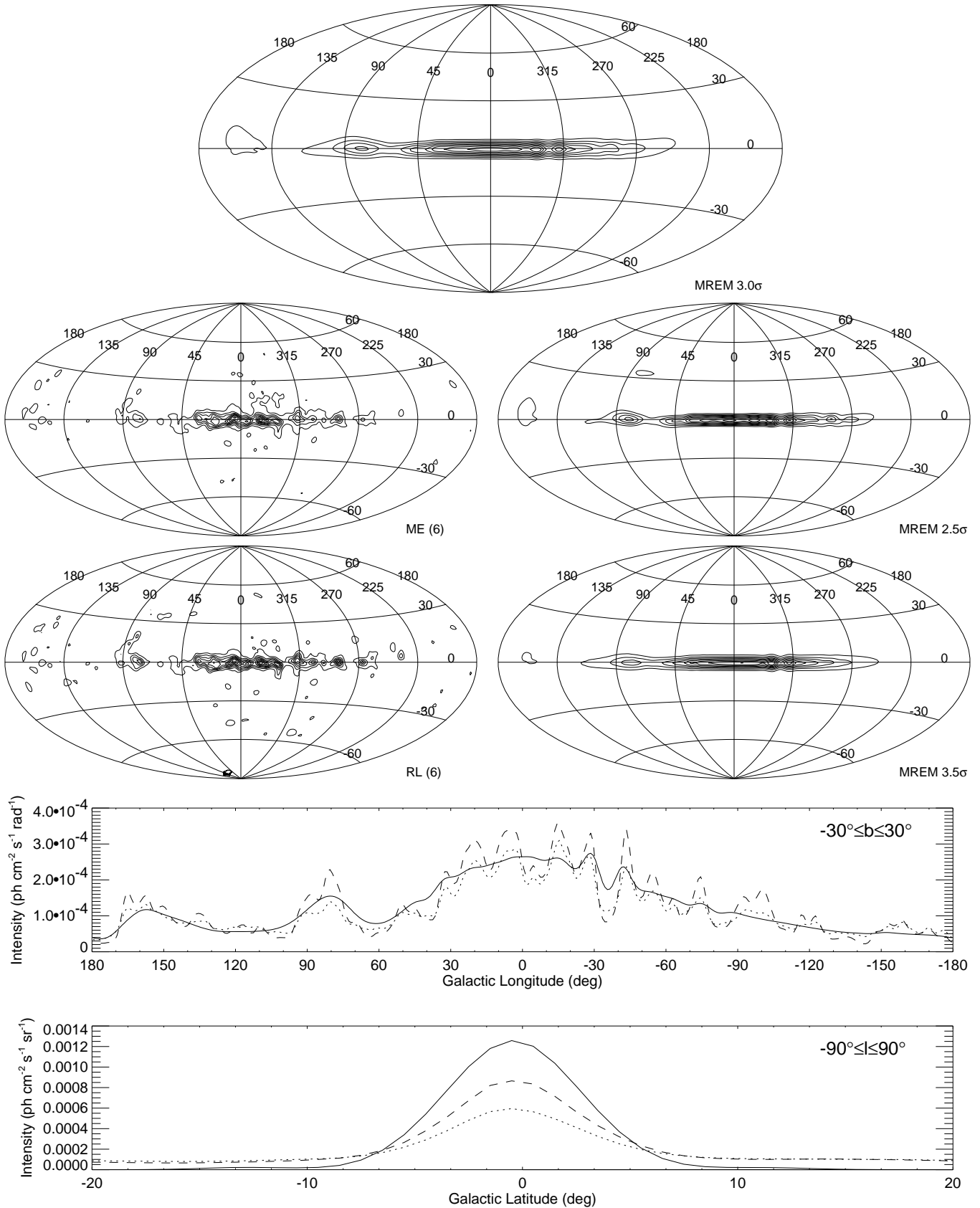


Fig. 6. COMPTEL 1.8 MeV all-sky maps derived using the maximum entropy method (ME), the Richardson-Lucy algorithm (RL), and the Multiresolution Expectation Maximization algorithm (MREM). In the profiles, the MREM ($s = 3.0$) reconstruction is shown as solid, the ME reconstruction as dotted, and the RL reconstruction as dashed line.

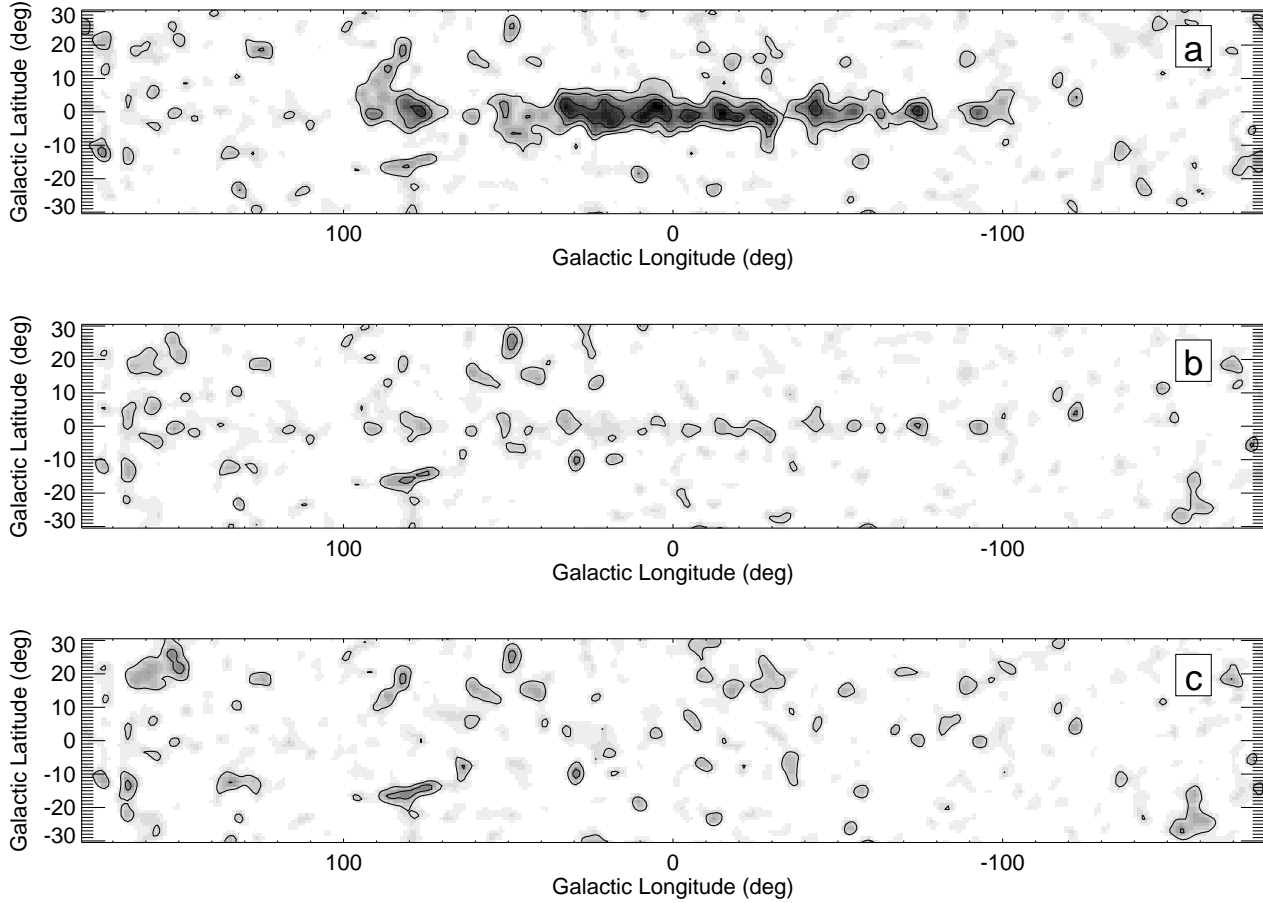


Fig. 7. Residual maximum likelihood ratio maps of the COMPTEL 1.8 MeV all-sky maps. Contour levels like in Fig. 2. From top to bottom the panels show (a) the residuals of iteration 6 of the ME reconstruction, (b) the residuals of iteration 6 of the RL reconstruction, and (c) the residuals of the MREM ($s = 3.0$) reconstruction.

MeV latitude profile (7.5° FWHM) is even smaller than that obtained for the exponential disk simulation (8.8° FWHM), indicating that the scale height of the ^{26}Al distribution may be even below 90 pc.

Near the anticentre, all maps of Fig. 6 show indications for extended 1.8 MeV γ -ray line emission. In the ME and RL reconstructions, weak emission spots are spread over a region extending from $125^\circ - 170^\circ$ in galactic longitude and from $-20^\circ - 30^\circ$ in galactic latitude. The MREM algorithm combines these spots to a more concentrated emission structure, roughly located at $l \sim 160^\circ$ with an angular extent of $\sim 20^\circ$. This again illustrates that the spots in the ME and RL images are not significant for themselves, but when combined they provide a significant 1.809 MeV emission feature.

Residual maximum likelihood ratio maps of the COMPTEL 1.8 MeV all-sky maps are compiled in Fig. 7. The ME reconstruction shows significant residual emission along the galactic plane which is strongly correlated to the reconstructed sky intensity distribution. The intensity profiles in Fig. 6 illustrate that iteration 6 of the ME recon-

struction considerably underestimates 1.8 MeV intensities with respect to RL and MREM. For higher ME iterations, this underestimation disappears as the maximum entropy reconstruction approaches the maximum likelihood solution. Yet, the diffuse intensity distribution breaks up into nearly isolated point sources for late iterations due to overfit of the data (Knödlseider et al. 1996). Therefore we typically present COMPTEL ME images and longitude profiles from ‘early’ iterations in order not to emphasise artificial structures, while ‘late’ iterations are used to derive 1.809 MeV fluxes and latitude profiles in order to recover the correct flux values (Diehl et al. 1995; Oberlack et al. 1996). Alternatively, intensity distributions for ‘late’ iterations have been smoothed to the instrumental resolution for image presentation to reduce the artificial lumpiness (Oberlack 1997; Strong et al. 1999).

Also the RL reconstruction shows residuals that are correlated with the galactic plane, although they are much smaller than for ME. Yet there are regions where almost no residuals are found, in particular at negative galactic longitudes ($l < 0^\circ$) above and below the galactic plane.

Comparison with the simulations suggests that the lack of residuals is again due to overfit of the data. In contrast, the MREM ($s = 3.0$) reconstruction provides residuals that appear uncorrelated with the galactic plane. This clearly illustrates that the MREM map presents a statistical satisfactory description of COMPTEL 1.8 MeV data.

5. Conclusions

An alternative imaging method for COMPTEL γ -ray data is presented, using a newly developed multiresolution reconstruction algorithm based on wavelets. The maximum entropy and Richardson-Lucy algorithms, which have been used previously for COMPTEL image reconstruction, are very sensitive to statistical noise in the data, leading to image lumpiness and ‘hot spots’ in the reconstructed intensity maps. In particular, artificial ‘hot spots’ are indistinguishable from real point sources on basis of the sky maps alone, requiring a substantial additional analysis effort to assess their reality. We present the resulting reconstructed image of the 1.809 MeV sky as an alternative view, complementing previously presented images from the other methods, and pointing out their limitations. In particular, we caution to overinterpret structure in the ME and RL sky maps when modelling the galactic ^{26}Al emission for other studies (e.g. Lentz et al. 1998).

Applying our new algorithm to COMPTEL data largely reduces or even removes artificial ‘hot spots’ and image lumpiness, depending on the selected significance requirement s . Simulations indicate that $s = 3.0$ seems to provide a reasonable choice for the reconstruction: while artifacts are mainly removed from the image, hints for weak ($3 - 4\sigma$) point sources are still present. Nevertheless, it should be clear that the MREM sky map obtained in this work not necessarily provides a realistic view of the 1.809 MeV sky. The real 1.809 MeV intensity profile is probably much more confined to the galactic plane than the emission in the MREM sky map, but with an angular resolution of 4° (FWHM), COMPTEL is not capable of resolving this confinement. The 1.809 MeV emission along the galactic plane may be much more structured than shown in the MREM map, but the sensitivity of COMPTEL is not sufficient to map this structure. In this sense, MREM provides a more reliable image of the 1.809 MeV γ -ray sky with respect to ME and RL since it does not show emission structures for which there is no strong evidence. Weak emission features which are close to the sensitivity limit of COMPTEL may however be suppressed in the MREM maps. Therefore ME and RL maps are used as complementary analysis tools.

Acknowledgements. JK is supported by the European Community through grant number ERBFMBICT 950387. The COMPTEL project is supported by the German government through DARA grant 50 QV 90968, by NASA under contract NAS5-26645, and by the Netherlands Organisation for Scientific Research NWO. This research has made use of data obtained

through the High Energy Astrophysics Science Archive Research Center Online Service, provided by the NASA/Goddard Space Flight Center.

References

- Bennett, C. L., Smoot, G. F., Hinshaw, G., et al. 1992, ApJ, 396, L7
- Bloemen, H., Collmar, W., Diehl, R., et al. 1999a, in Proc. 3rd INTEGRAL Workshop, Taormina (Gordon & Breach), in press
- Bloemen, H., Diehl, R., Hermsen, W., Knödlseider, J., Schönfelder, V. 1999b, in Proc. 3rd INTEGRAL Workshop, Taormina (Gordon & Breach), in press
- Coifman, R. R., & Donoho, D. L. 1995, in Wavelet and Statistics, eds. A. Antoniadis, and G. Oppenheim, (Lecture Notes in Statistics, Vol. 103)
- de Boer, H., Bennett, K., den Herder, J. W., et al. 1992, in Data Analysis in Astronomy Vol. IV, ed. V. Di. Gesù, Plenum Press (New York), 241
- Dempster, A. P., Laird, N. M., Rubin, D. B. 1977, J. Royal Stat. Soc. Ser. B, 39, 1
- Diehl, R., Dupraz, C., Bennett, K., et al. 1995, A&A, 298, 445
- Diehl, R., Oberlack, U., Knödlseider, J., et al. 1997, in Proc. of the Fourth Compton Symposium, eds. C. D. Dermer, M. S. Strickman, and J. D. Kurfess (AIP), 1114
- Donoho, D. L. 1993, in Proceedings of Symposia in Applied Mathematics, Vol. 47, p. 173
- Fessler, J. A., & Hero, A. O. 1994, technical report Univ. of Michigan, Comm. and Sign. Proc. Lab., Dept. of EECS,
- Graps, A. 1995, IEEE Computational Science and Engineering 2, 50
- Kaufman, L. 1987, IEEE Trans. Med. Img., 6, 37
- Knödlseider, J., von Ballmoos, P., Diehl, R., et al. 1996, SPIE Vol. 2806, 386
- Knödlseider, J. 1997, Ph. D. thesis, Univ. Paul Sabatier, Toulouse, available at <http://www.cesr.fr/~jurgen/publications.html>
- Knödlseider, J., Bennett, K., Bloemen, H., et al. 1999, A&A, in press
- Lentz, E. J., Branch, D., & Baron, E. 1998, astro-ph/9804115, submitted to ApJ
- Lucy, L. B. 1974, AJ, 79, 745
- Oberlack, U., Bennett, K., Bloemen, H., et al. 1996, A&AS, 120, 311C
- Oberlack, U. 1997, Ph. D. thesis, Technische Universität München, Munich, available at http://www.astro.columbia.edu/~oberlack/phd_thesis
- Piña, R. K., & Puetter, R. C. 1993, PASP, 105, 637
- Richardson, W. H. 1972, J. Opt. Soc. Am., 62, 55
- Schönfelder, V., Aarts, H., Bennett, K., et al. 1993, ApJS, 86, 657
- Shepp, L. A., & Vardi, Y. 1982, IEEE Trans. Med. Img., 1, 113
- Strong, A. W., Cabeza-Orcel, P., Bennett, K., et al. 1992, in Data Analysis in Astronomy IV, ed. Di Gesù et al., Plenum Press (New York), 251
- Strong, A., et al. 1999, in Proc. 3rd INTEGRAL Workshop, Taormina (Gordon & Breach), in press